




Rationally designed transition metal hydroxide nanosheet arrays on graphene for artificial CO₂ reduction

Kang-Qiang Lu^{1,2}, Yue-Hua Li^{1,2}, Fan Zhang¹, Ming-Yu Qi^{1,2}, Xue Chen^{1,2}, Zi-Rong Tang¹, Yoichi M. A. Yamada ³, Masakazu Anpo^{1,4}, Marco Conte ⁵ & Yi-Jun Xu ^{1,2}✉

The performance of transition metal hydroxides, as cocatalysts for CO₂ photoreduction, is significantly limited by their inherent weaknesses of poor conductivity and stacked structure. Herein, we report the rational assembly of a series of transition metal hydroxides on graphene to act as a cocatalyst ensemble for efficient CO₂ photoreduction. In particular, with the Ru-dye as visible light photosensitizer, hierarchical Ni(OH)₂ nanosheet arrays-graphene (Ni(OH)₂-GR) composites exhibit superior photoactivity and selectivity, which remarkably surpass other counterparts and most of analogous hybrid photocatalyst system. The origin of such superior performance of Ni(OH)₂-GR is attributed to its appropriate synergy on the enhanced adsorption of CO₂, increased active sites for CO₂ reduction and improved charge carriers separation/transfer. This work is anticipated to spur rationally designing efficient earth-abundant transition metal hydroxides-based cocatalysts on graphene and other two-dimension platforms for artificial reduction of CO₂ to solar chemicals and fuels.

¹College of Chemistry, New Campus, Fuzhou University, 350116 Fuzhou, P. R. China. ²State Key Laboratory of Photocatalysis on Energy and Environment, College of Chemistry, Fuzhou University, 350116 Fuzhou, P. R. China. ³RIKEN Center for Sustainable Resource Science, Hirosawa, Wako, Saitama 351-0198, Japan. ⁴Department of Applied Chemistry, Graduate School of Engineering, Osaka Prefecture University, Osaka 599-8531, Japan. ⁵Department of Chemistry, University of Sheffield, Sheffield S3 7HF, UK. ✉email: yjxu@fzu.edu.cn

Arificial photoreduction of carbon dioxide (CO₂) into useful chemical feedstocks offers a promising and sustainable long term solution to the issues of increasing energy demands and climate change^{1–6}. Nevertheless, there is still a long way to achieve efficient and selective photocatalytic CO₂ reduction, especially in diluted CO₂, which is primarily because of the low CO₂ adsorption, high recombination rate of charge carriers in photocatalysts, concealed active sites, and the competing H₂ evolution reaction^{7–11}. To overcome these limitations, rational construction of hybrid photocatalytic systems, in which photosensitizers and cocatalysts operate in a harmonious manner, has arisen as a promising approach^{12–16}.

Recently, the earth-abundant transition metal hydroxides, especially Ni(OH)₂, as cocatalysts for photocatalytic CO₂ reduction, have attracted extensive research interests due to their low cost, easy preparation, and effective adsorption for CO₂^{2,17}. However, the charge transfer efficiency of Ni(OH)₂ is inferior because of its inherent weakness of poor conductivity, which results in the net efficiency of Ni(OH)₂ in improving the photoactivity is often limited^{18,19}. An effective way to overcome this disadvantage could be incorporating Ni(OH)₂ with electrically conductive graphene (GR)^{1,20}. In addition, the two-dimensional (2D) GR nanosheets with a large π -conjugated structure can further enhance the adsorption of CO₂ via interacting with delocalized π -conjugation binding π_3^* of CO₂ molecule^{21,22}. Moreover, the large 2D platform and amenable wet-chemistry processability of GR also benefit the controllable composite structure construction^{1,23–25}. In particular, rationally constructing nanoarray gradient structures based on vertical sheets-on-sheets is potentially able to harmoniously exert the synergistic ensemble effects of accelerating separation/transfer of charge carriers and exposing open active sites for the efficient adsorption, activation, and photoreduction of CO₂^{18,26,27}.

Herein, we report the facile synthesis of a series of different transition metal hydroxides, including Ni(OH)₂, Fe(OH)₃, Cu(OH)₂, and Co(OH)₂, onto the 2D platform of GR to act as cocatalysts ensemble for CO₂ photoreduction to solar fuels. With the Ru-dye as a visible-light photosensitizer, the optimal hierarchical Ni(OH)₂-10%GR nanosheet arrays composite exhibits superior activity and selectivity, achieving a high CO formation rate of 10725 $\mu\text{mol h}^{-1} \text{g}^{-1}$ and selectivity of 96% in pure CO₂. More importantly, even in diluted CO₂ (10% CO₂, representative CO₂ concentration of waste gas from coal-fired power stations)⁷, this Ni(OH)₂-10%GR composite still demonstrates the excellent performance with CO production rate of 7432 $\mu\text{mol h}^{-1} \text{g}^{-1}$ and high selectivity of 92%, which significantly surpasses other counterparts including bare Ni(OH)₂, Ni(OH)₂ nanoparticles-graphene (Ni(OH)₂ NPs-GR), Fe(OH)₃-GR, Cu(OH)₂-GR and Co(OH)₂-GR and outperforms most of analogous hybrid cocatalysts system in literatures. The underlying origin for such superior visible-light photoactivity and selectivity over Ni(OH)₂-10%GR has been credited for its appropriate synergy on the effective adsorption of CO₂, enriched active sites for CO₂ reduction, and excellent charge carriers separation and transfer. It is hoped that this work would provide instructive guideline for rational design of earth-abundant transition metal hydroxides-based cocatalysts by harnessing the rich surface chemistry of GR and other 2D materials platforms toward efficient and selective solar light driven CO₂ reduction to value-added fuels and chemicals in a sustainable way.

Results

Synthesis and morphology. As shown in Fig. 1a, the growth of transition metal hydroxides on the GR platform can be obtained via in situ heterogeneous nucleation and subsequent oriented crystal growth in solution phase. After transition metal precursor

adding into the graphene oxide (GO) solution, the strong electrostatic interaction between negatively GO (Supplementary Fig. 1 and Supplementary Note 1) and transition metal cations (Ni²⁺, Fe³⁺, Cu²⁺, Co²⁺) leads to a firm adsorption of transition metal cations on the surface of GO²¹. At the beginning of the growth process, hexamethylenetetramine (HMTA) as a hydrolyzing agent can tardily decompose to liberate OH⁻ ions, and then transition metal cations react with OH⁻ ions to form dense transition metal hydroxides nuclei on the surface of GO^{17,28}. The high density of transition metal hydroxide nuclei conduce to the vertical growth of nanosheets because the steric hindrance from adjacent seeds can hinder the in-plane direction growth²⁹. Meanwhile, the GO precursor can also be reduced to GR during the thermal reflux process^{1,20}, by which different transition metal hydroxide-GR composites are formed.

Since the Ni(OH)₂-10%GR composite exhibits the optimal photocatalytic performance among the as-obtained transition metal hydroxide-GR composites as shown in the section of CO₂ photoreduction, the following discussion will mainly focus on the characterizations of Ni(OH)₂-10%GR composite. As shown in Supplementary Fig. 2 and Supplementary Note 2, the morphological evolution process of Ni(OH)₂-10%GR has been investigated via time-dependent SEM images. It can be seen that GO surface is smooth before the refluxing reaction. As refluxing time increases, Ni(OH)₂ gradually nucleates and grows on the GR surface, which makes GR surface become rough, and when the refluxing time is prolonged to 7 h, Ni(OH)₂ nanosheet arrays structure begins to form on the GR surface. After refluxing for 10 h, the surface of GR is covered with homogeneous Ni(OH)₂ nanosheet arrays as revealed by the SEM images in Fig. 1b, c. In addition, as shown in Supplementary Fig. 3, the thickness of the Ni(OH)₂ layers in Ni(OH)₂-10%GR composite can be found to be ca. 10 nm. Notably, it is pivotal to regulate the amount of GR to achieve such evenly dispersed hierarchical Ni(OH)₂ nanosheet arrays on the GR platform because the amount of GR affects the morphology of Ni(OH)₂-GR hybrids significantly. As shown in Supplementary Fig. 4, when the amount of GR is 1 wt% or 5 wt%, stacked Ni(OH)₂ nanosheet arrays are obtained whereas nanosheet array structures cannot be formed when the amount of GR is 30 wt% or 50 wt%. In addition, in the absence of GR, the as-obtained blank Ni(OH)₂ displays a sphere-like aggregated structure (Supplementary Fig. 5), which is because the nucleus formation and growth of blank Ni(OH)₂ lack steric hindrance, thereby leading to an omnidirectional and superimposed assembly²³.

As shown in Fig. 1d, the hierarchical nanosheet array structure of Ni(OH)₂-10%GR is further confirmed by transmission electron microscopy (TEM) characterization. In addition, as shown in Fig. 1e and Supplementary Fig. 6, because the α -Ni(OH)₂ is sensitive to electron-beam irradiation, only high-resolution TEM image of NiO evolved from the α -Ni(OH)₂ has been caught (Supplementary Note 3)^{30–33}. Furthermore, elemental mapping images of Ni(OH)₂-10%GR hybrid in Fig. 1f show the spatial distributions of C, O, and Ni, indicating the uniform growth of Ni(OH)₂ nanosheet arrays on the matrix of GR. Furthermore, to determine the length of Ni(OH)₂ nanosheet arrays, atomic force microscopy (AFM) of the Ni(OH)₂-10%GR hybrid has been conducted. As displayed in Fig. 1g and Supplementary Fig. 7, the topography of Ni(OH)₂-10%GR composite shows a 2D lamellar structure with a thickness of ca. 60 nm. Considering the thickness of GR sheet (0.9 nm)³⁴ and the growth of Ni(OH)₂ on both sides of GR, the length of Ni(OH)₂ nanosheet arrays is deduced to be about 30 nm.

Structure characterization. X-ray diffraction (XRD) was used to characterize the crystal structures of these as-synthesized samples.

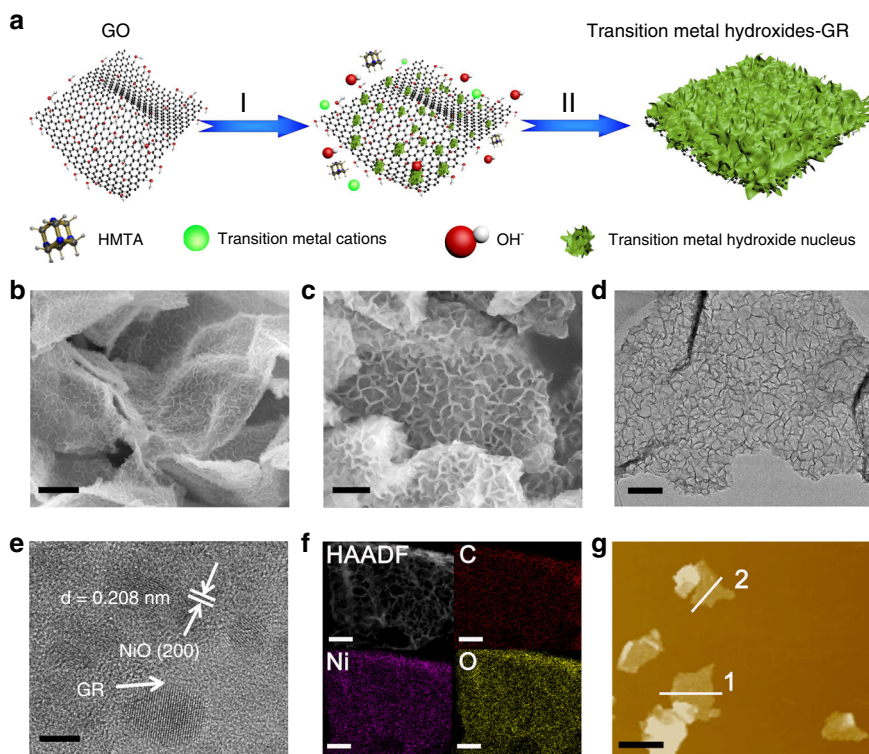


Fig. 1 Synthesis and morphology characterization. **a** Schematic illustration of synthesis procedure for transition metal hydroxides onto the GR platform. I in situ heterogeneous nucleation, II oriented crystal growth. **b, c** FESEM images, **d** TEM image, **e** HRTEM image, **f** elemental mapping results, and **g** AFM image of the Ni(OH)₂-10%GR. The scale bar are 500 nm in **b**, 200 nm in **c**, 100 nm in **d**, 2 nm in **e**, 1 μm in **f**, 3 μm in **g**.

As shown in Fig. 2a, the diffraction peaks of Ni(OH)₂ at 8.7°, 17.3°, 33.4°, and 59.9° can be indexed to (003), (006), (101), and (110) planes of α-Ni(OH)₂ (JCPDS no. 38-0715)^{28,35}. Two peaks at low angles (<20°) clearly indicate the layered structure of Ni(OH)₂³². Notably, the positions of (003) and (006) diffraction peaks shift towards lower angle as compared to that of standard card, indicating enlarged interlayer spacing of as-obtained Ni(OH)₂, which has been widely reported in the previous literatures^{32,36,37}. In addition, Ni(OH)₂-GR hybrids exhibit analogous XRD patterns to that of the blank Ni(OH)₂. The diffraction peaks of GR (Supplementary Fig. 8) have not been observed in these composites, which could be because GR layers are densely wrapped by Ni(OH)₂ nanosheet arrays^{18,23}. The analysis of Raman spectroscopy in Fig. 2b shows that peaks at 1353 and 1590 cm⁻¹ are assigned to the D-band and G-band of GR, and the peak at 468 cm⁻¹ is ascribed to Ni(OH)₂^{28,38}. The well-identified Ni(OH)₂ and GR peaks in Ni(OH)₂-10%GR composite indicate that Ni(OH)₂ nanosheet arrays have successfully grown on the GR platform. Notably, the I_D/I_G ratio is 0.97 for Ni(OH)₂-10%GR, which is lower than 1.01 for GO, indicating that the thermal reduction process enhances the graphitization of GR³⁴. Chemical composition and elemental states of Ni(OH)₂-10%GR composite have been further monitored by X-ray photoelectron spectroscopy (XPS). The survey XPS spectrum in Fig. 2c confirms the existing elements of C, Ni and O in Ni(OH)₂-10%GR composite. In addition, compared with C 1s spectrum of original GO in Supplementary Fig. 9, the C 1s spectrum of Ni(OH)₂-10%GR hybrid shows an obvious loss of oxygenated functional groups, confirming the effective reduction of GO to GR during the thermal reflux process (Fig. 2d)^{39,40}. Furthermore, in the Ni 2p region of Ni(OH)₂-10%GR composite (Fig. 2e), peaks of Ni 2p_{3/2} and Ni 2p_{1/2} are at 855.9 and 873.5 eV, which indicates that the Ni species are in +2 valence state^{17,35,41}. In addition, two shoulder peaks at 861.4 and 879.5 eV are related to the satellite

peaks of Ni 2p_{3/2} and Ni 2p_{1/2}⁷. The O 1s spectrum in Fig. 2f displays a typical peak at 531.2 eV, which can be ascribed to the Ni-OH bond in Ni(OH)₂-10%GR composite¹⁸. The peak situated at 533.3 eV is assigned to the adsorbed H₂O molecules^{30,42}. Moreover, as shown in Supplementary Fig. 10 and Supplementary Note 4, the thermogravimetric (TG) analysis demonstrates that the actual content of GR in the Ni(OH)₂-10%GR hybrid is ca. 10.3 wt%, which almost equals to the feedstock proportion.

Photoreduction CO₂ performance. The visible-light-driven photocatalytic CO₂ reduction reactions were performed in a catalytic system with [Ru(bpy)₃]Cl₂·6H₂O (abbreviated as Ru) as photosensitizer and triethanolamine (TEOA) as electron donor. Acetonitrile (MeCN) is selected as a reaction solvent because of its high solubility for CO₂. CO and H₂ are detected as the main gas phase products and no liquid phase products (e.g., HCHO, CH₃OH, and HCOOH) are detected (Supplementary Fig. 11 and Supplementary Note 5). As displayed in Fig. 3a, in the presence of Ru alone, low CO evolution rate (187 μmol h⁻¹ g⁻¹) and selectivity (67%) are achieved in pure CO₂, which is due to the poor charge transfer efficiency and lack of surface active sites^{8,43,44}. The addition of Ni(OH)₂ cocatalyst into the Ru solution leads to a significant improvement of photocatalytic performance. The rate of evolved CO reaches a value of 4492 μmol h⁻¹ g⁻¹ with CO selectivity of 87%, which indicates that Ni(OH)₂ is an effective cocatalyst for photocatalytic CO₂ reduction. Further improvements of photocatalytic activity and selectivity have been achieved after compositing Ni(OH)₂ nanosheet arrays with electrically conductive GR. As shown in Supplementary Fig. 12 and Supplementary Note 6, when the content of GR is 10%, the Ni(OH)₂-10%GR composite shows the optimal photocatalytic performance, achieving the CO formation rate of 10725 μmol h⁻¹ g⁻¹, which is ~2.3 and 57.2 times as high as that of blank Ni(OH)₂ and bare Ru, respectively. The apparent quantum efficiency (AQE) for CO formation at 450 nm is

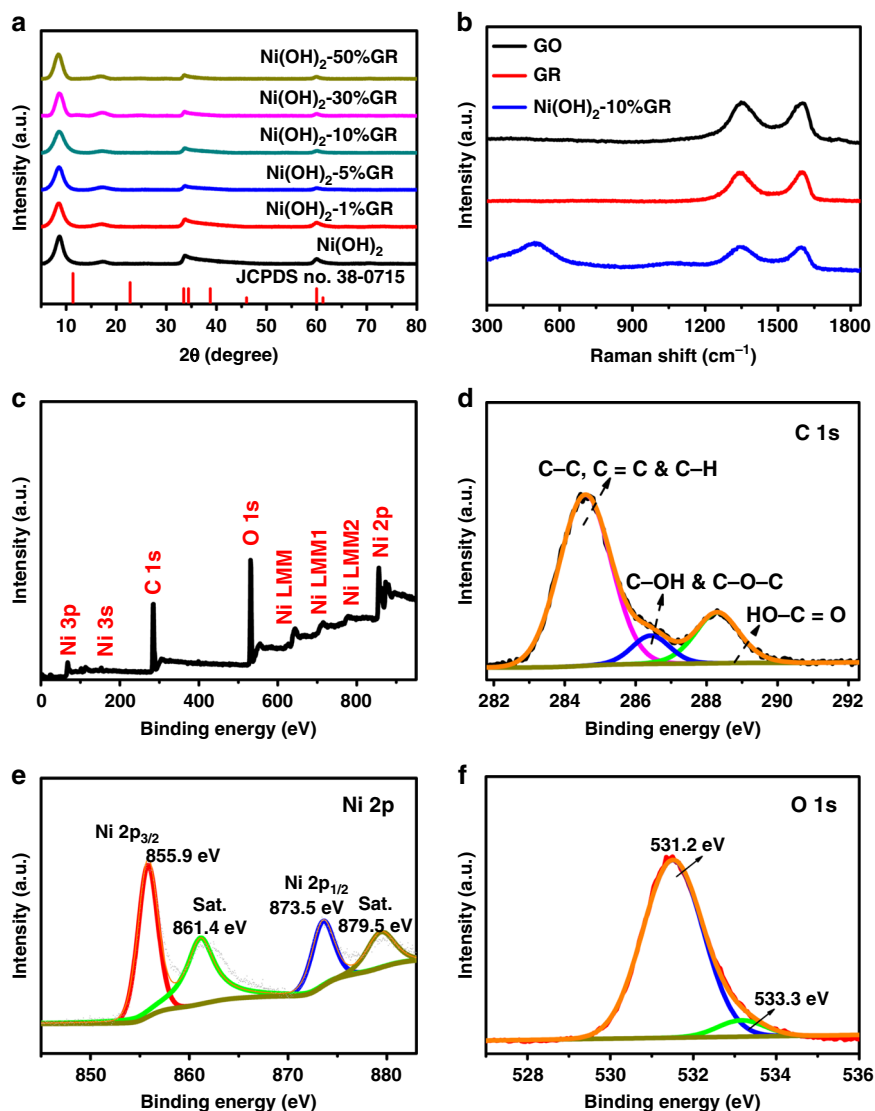


Fig. 2 Structure characterization of $\text{Ni}(\text{OH})_2\text{-10\%GR}$. **a** XRD patterns of $\text{Ni}(\text{OH})_2\text{-GR}$ composite with different GR contents and bare $\text{Ni}(\text{OH})_2$. **b** Raman spectra of GO, GR and $\text{Ni}(\text{OH})_2\text{-10\%GR}$. **c** XPS survey spectrum, high-resolution XPS spectra of **d** C 1s, **e** Ni 2p, and **f** O 1s of $\text{Ni}(\text{OH})_2\text{-10\%GR}$.

calculated to be 1.03%. In addition, the $\text{Ni}(\text{OH})_2\text{-10\%GR}$ hybrid exhibits a superior selectivity of 96% for photocatalytic CO_2 to CO reduction. Moreover, as shown in Supplementary Table 1, it can be found that the photocatalytic activity and selectivity of $\text{Ni}(\text{OH})_2\text{-10\%GR}$ composite in pure CO_2 has exceeded that of most recently reported cocatalysts. Furthermore, $\text{Ni}(\text{OH})_2$ nanoparticles-graphene ($\text{Ni}(\text{OH})_2$ NPs-10%GR) hybrid has also been synthesized for a comparative study (Supplementary Figs. 13–15 and Supplementary Note 7–9). As demonstrated in Fig. 3a, the $\text{Ni}(\text{OH})_2$ NPs-10%GR composite exhibits lower photocatalytic activity (CO formation rate of $6742 \mu\text{mol h}^{-1} \text{g}^{-1}$) and CO selectivity (90%) than that of the $\text{Ni}(\text{OH})_2\text{-10\%GR}$ hybrid, which indicates that constructing hierarchical nanosheet array structure is an effective way to improve photocatalytic performance of the transition metal hydroxide-GR composite.

To assess the practical application of the obtained catalysts, we further perform the CO_2 reduction reaction in diluted CO_2 (10% CO_2 , representative CO_2 concentration of waste gas from coal-fired power stations)⁴⁵. As demonstrated in Fig. 3b, $\text{Ni}(\text{OH})_2\text{-10\%GR}$ composite displays a superior photocatalytic activity with the CO formation rate of $7432 \mu\text{mol h}^{-1} \text{g}^{-1}$, corresponding to AQE

of 0.95% at 450 nm. Significantly, $\text{Ni}(\text{OH})_2\text{-10\%GR}$ still exhibits a high CO selectivity of 92% in diluted CO_2 . As shown in Supplementary Table 2, the photocatalytic performance of $\text{Ni}(\text{OH})_2\text{-10\%GR}$ hybrid in diluted CO_2 is also superior than that of most previously reported results regarding analogous hybrid photocatalyst system in literatures. In addition, the photocatalytic activity and selectivity of $\text{Ni}(\text{OH})_2\text{-10\%GR}$ hybrid are much higher than that of blank $\text{Ni}(\text{OH})_2$ (CO generation rate of $1717 \mu\text{mol h}^{-1} \text{g}^{-1}$ and selectivity of 64%) and $\text{Ni}(\text{OH})_2$ NPs-10%GR counterpart (CO formation rate of $4890 \mu\text{mol h}^{-1} \text{g}^{-1}$ and selectivity of 85%) in diluted CO_2 .

The photocatalytic performance of other transition metal hydroxide-GR ($\text{Fe}(\text{OH})_3\text{-GR}$, $\text{Cu}(\text{OH})_2\text{-GR}$ and $\text{Co}(\text{OH})_2\text{-GR}$) composites have also been tested for comparison under identical reaction conditions (Supplementary Figs. 16–18, Supplementary Notes 10 and 11). Similar to $\text{Ni}(\text{OH})_2\text{-GR}$ composites, $\text{Fe}(\text{OH})_3\text{-GR}$, $\text{Cu}(\text{OH})_2\text{-GR}$, and $\text{Co}(\text{OH})_2\text{-GR}$ composites also exhibit the optimal photocatalytic performance when the content of GR is 10%. As displayed in Fig. 3a, b, $\text{Ni}(\text{OH})_2\text{-10\%GR}$ or $\text{Ni}(\text{OH})_2$ NPs-10%GR composite shows obviously higher photoactivity and selectivity than that of $\text{Fe}(\text{OH})_3\text{-10\%GR}$ and $\text{Cu}(\text{OH})_2\text{-10\%GR}$ in

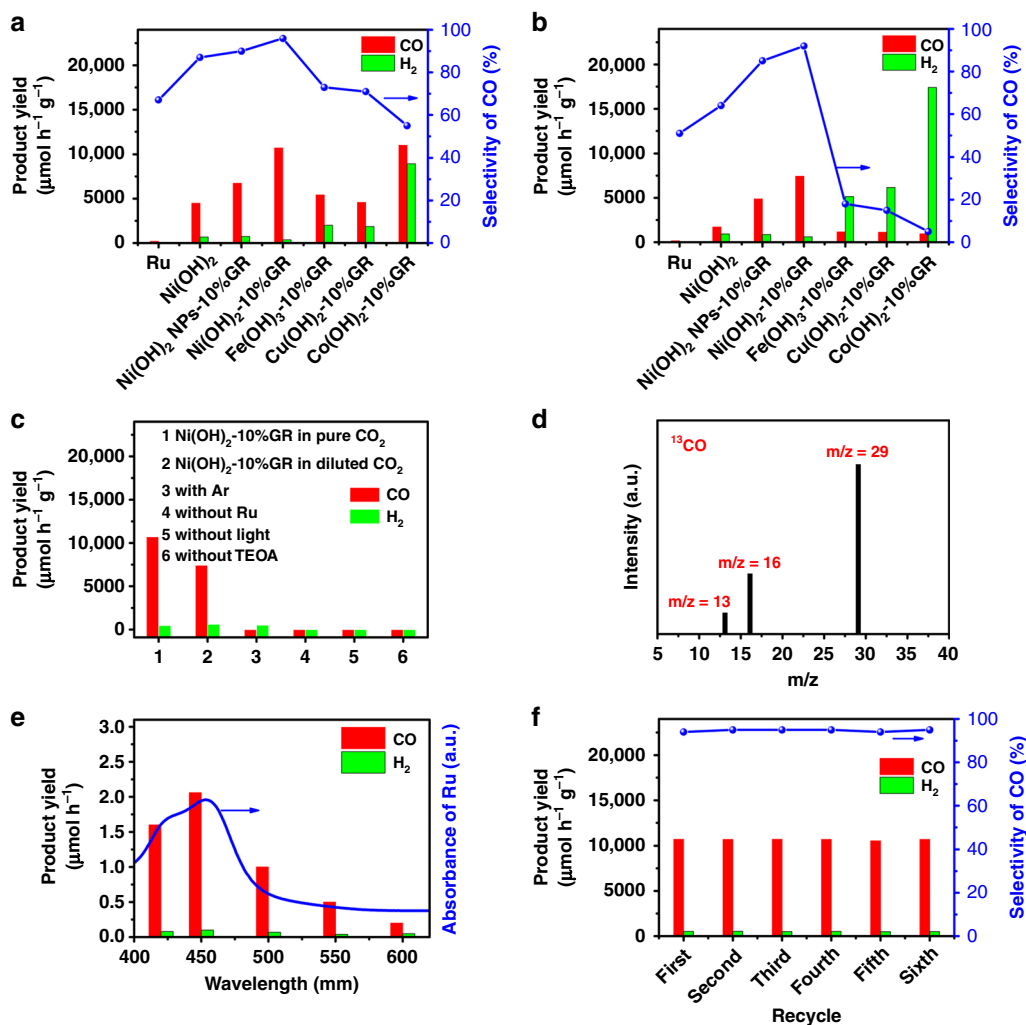


Fig. 3 The photocatalytic performance of CO₂ reduction. CO₂ photoreduction performance over Ru, Ni(OH)₂, Ni(OH)₂ NPs-10%GR, Ni(OH)₂-10%GR, Fe(OH)₃-10%GR, Cu(OH)₂-10%GR, and Co(OH)₂-10%GR **a** in pure CO₂ and **b** in diluted CO₂. **c** CO₂ photoreduction performance under various reaction conditions. **d** Mass spectrum of ¹³CO (m/z = 29) produced over Ni(OH)₂-10%GR in the photocatalytic reduction of ¹³CO₂. **e** Wavelength dependence of the yields of CO and H₂ over Ni(OH)₂-10%GR, and the light absorption spectrum of the Ru photosensitizer. **f** Recycling test of Ni(OH)₂-10%GR.

both pure CO₂ and diluted CO₂. Notably, Co(OH)₂-10%GR shows a CO production rate of 11625 μmol h⁻¹ g⁻¹ in pure CO₂, which is slightly higher than that of Ni(OH)₂-10%GR. However, the CO selectivity over Co(OH)₂-10%GR only reaches 56%. Moreover, the CO formation rate of Co(OH)₂-10%GR dramatically declines to 945 μmol h⁻¹ g⁻¹ with a low CO selectivity of 4% in diluted CO₂. These results clearly demonstrate that Ni(OH)₂ is a more efficient and selective cocatalyst for photocatalytic reduction of CO₂ to CO than other transition metal hydroxides.

To further study the factors that could influence the performance of photocatalysts, a series of control experiments are conducted. As displayed in column 3 of Fig. 3c, the comparative reaction in pure argon (Ar) indicates that only slight H₂ is produced and no CO is formed. In addition, isotopic experiment with ¹³CO₂ as substrate has also been carried out to confirm the origin of CO. As displayed in Fig. 3d, the mass spectrum signal of ¹³CO (m/z = 29) is clearly detected. These results definitely confirm that CO indeed derives from the photocatalytic reduction of CO₂⁴⁶. In addition, as shown in column 4–6 of Fig. 3c, control experiments in the absence of Ru or visible-light irradiation or TEOA result in the formation of a trace amount of CO and H₂, which confirms that the CO₂ reduction is driven by visible-light irradiation and the sacrificial agent is of great significance. Moreover, as shown in Fig. 3e, the wavelength

dependency of CO production shows that the tendency of CO generation matches well with the absorption spectrum of Ru photosensitizer, further confirming that the photocatalytic CO₂ reduction is indeed driven by the absorbed photon of Ru⁴⁷. Furthermore, the stability of Ni(OH)₂-10%GR cocatalyst has been evaluated by cycle experiments. The result in Fig. 3f shows that the photoactivity loss over Ni(OH)₂-10%GR composite is negligible after six consecutive cycles. In addition, as shown in Supplementary Figs. 19 and 20, the results of XRD and XPS over fresh and used Ni(OH)₂-10%GR show the same crystalline phase structure and element composition. SEM and TEM images of the used Ni(OH)₂-10%GR sample in Supplementary Fig. 21 also indicate no obvious structural change after visible light illumination for 12 h. These results clearly demonstrate that Ni(OH)₂-10%GR is a stable cocatalyst for photocatalytic CO₂ reduction under present conditions. In addition, the turnover number (TON) for CO formation respect to Ru atoms is 4.8 over 5 h of stable operation, reflecting the catalytic nature of the reaction. Notably, this TON value is higher than that of previously reported ruthenium-nickel molecular photocatalysts^{48,49}.

Mechanism of enhanced photocatalytic performance. To reveal the origin of the enhanced photocatalytic performance of Ni(OH)₂-10%GR composite compared to that of other

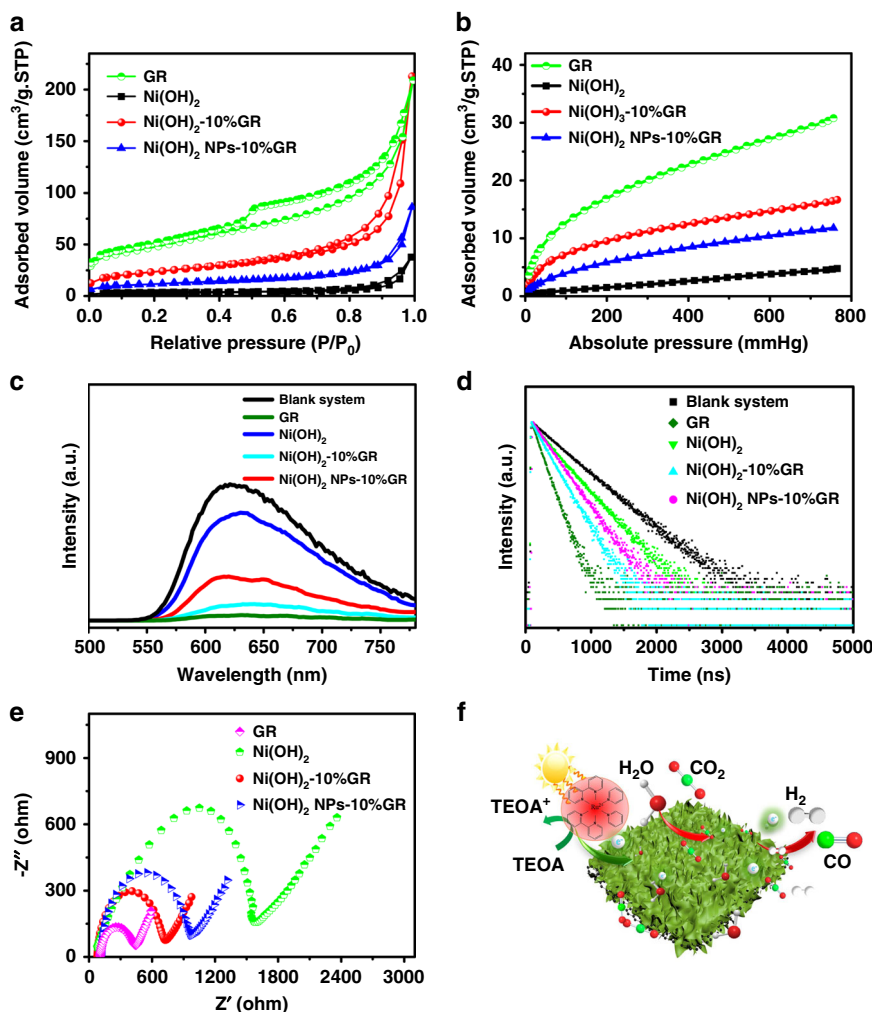


Fig. 4 CO_2 adsorption and photoelectrical properties of various photocatalysts. **a** N_2 adsorption-desorption isotherms and **b** CO_2 adsorption isotherms of GR, $\text{Ni}(\text{OH})_2$, $\text{Ni}(\text{OH})_2$ NPs-10%GR and $\text{Ni}(\text{OH})_2$ -10%GR. **c** Steady-state PL spectra and **d** time-resolved PL spectra decay of the photocatalytic CO_2 reduction systems with cocatalysts of GR, $\text{Ni}(\text{OH})_2$, $\text{Ni}(\text{OH})_2$ NPs-10%GR, $\text{Ni}(\text{OH})_2$ -10%GR and without cocatalysts. **e** EIS Nyquist plots of GR, $\text{Ni}(\text{OH})_2$, $\text{Ni}(\text{OH})_2$ NPs-10%GR, and $\text{Ni}(\text{OH})_2$ -10%GR. **f** Proposed photocatalytic mechanism of $\text{Ni}(\text{OH})_2$ -10%GR with Ru photosensitizer for visible-light-driven photocatalytic CO_2 reduction reaction.

counterparts, various complementary characterizations have been conducted. Firstly, the surface areas and CO_2 uptake ability of these samples have been studied. As shown in Fig. 4a and Supplementary Table 3, the BET surface area of $\text{Ni}(\text{OH})_2$ -10%GR hybrid ($83 \text{ m}^2 \text{ g}^{-1}$) is obviously higher than that of blank $\text{Ni}(\text{OH})_2$ ($11 \text{ m}^2 \text{ g}^{-1}$) and $\text{Ni}(\text{OH})_2$ NPs-10%GR composite ($40 \text{ m}^2 \text{ g}^{-1}$), which clearly indicates that introducing GR into the composite to construct hierarchical nanosheet array structure is beneficial for increasing the specific surface area. The augmented surface area of $\text{Ni}(\text{OH})_2$ -10%GR composite indicates an increased exposed surface active sites and effective mass transportation of reactants and products, which are conducive to enhance the photocatalytic activity of the composite^{17,23}. In addition, the CO_2 adsorption isotherms of GR, $\text{Ni}(\text{OH})_2$, $\text{Ni}(\text{OH})_2$ -10%GR, and $\text{Ni}(\text{OH})_2$ NPs-10%GR composite have also been collected. As shown in Fig. 4b, it can be seen that GR has a strong adsorption capacity for CO_2 . After compositing $\text{Ni}(\text{OH})_2$ with GR, $\text{Ni}(\text{OH})_2$ -10%GR and $\text{Ni}(\text{OH})_2$ NPs-10%GR composites exhibit significantly improved CO_2 adsorption capacity compared to that of blank $\text{Ni}(\text{OH})_2$. Notably, the $\text{Ni}(\text{OH})_2$ -10%GR hybrid shows higher CO_2 adsorption capacity than that of $\text{Ni}(\text{OH})_2$ NPs-10%GR hybrid. Similar trends are also observed in CO_2 temperature-programmed desorption (TPD)

tests, as shown in Supplementary Fig. 22. These results suggest that the introduction of GR and construction of hierarchical nanosheet array structures can effectively enhance CO_2 adsorption capacity of the composite, which is desirable to facilitate the enrichment and activation of CO_2 molecule, thus contributing to the boosted photocatalytic performance of $\text{Ni}(\text{OH})_2$ -10%GR composite for CO_2 reduction^{12,44}.

On the other hand, photoluminescence (PL) and electrochemical impedance spectroscopy (EIS) measurements have been conducted to explore the separation and transfer process of charge carriers, which are another crucial factor affecting the photoactivity of CO_2 reduction^{7,44}. As shown in Fig. 4c, d and Supplementary Table 4, the cocatalysts contained systems show much lower PL intensities and shorter PL lifetimes than that of blank system. Generally, the lower PL emission intensity and shorter PL lifetime indicate the more efficient suppression of photoexcited charge recombination^{8,50}. In addition, as shown in Supplementary Fig. 23, there is almost no influence on the light absorption of Ru by the addition of $\text{Ni}(\text{OH})_2$ -10%GR cocatalyst, which further confirms that the quenching of PL intensity should be directly caused by the promoted transfer of photoexcited electrons⁵¹. Therefore, the introduction of

cocatalysts can effectively promote the separation of charge carriers in the CO₂ photoreduction system. Notably, compared with blank Ni(OH)₂ and Ni(OH)₂ NPs-10%GR contained systems, Ni(OH)₂-10%GR contained system exhibits significantly lower PL intensity and shorter PL lifetime, which validates that introduction of conductive GR into the composite for constructing hierarchical nanosheet array structures is able to effectively facilitate the separation of photogenerated charge carriers. In addition, as revealed in Fig. 4e, the EIS spectrum of Ni(OH)₂-10% GR displays a smaller semicircle in the Nyquist plot than that of blank Ni(OH)₂ and Ni(OH)₂ NPs-10%GR composite, which further confirms the elevated conductivity of the hybrid and the superiority of hierarchical nanosheet array structure in promoting the transfer of photogenerated charge carriers^{52,53}.

Previously reported theoretical calculations indicate that Ni sites possess stronger CO₂ adsorption affinity and weaker H⁺ affinity than that of other transition metal sites^{7,8,52}, which could be the main reason for the enhanced photocatalytic performance of Ni(OH)₂-10%GR composite compared to other transition metal hydroxide-GR composites (Fe(OH)₃-10%GR, Cu(OH)₂-10%GR, and Co(OH)₂-10%GR). As shown in Supplementary Fig. 24a, b, the enhanced CO₂ adsorption capacity of Ni(OH)₂-10%GR composite is confirmed by CO₂ adsorption isotherm and CO₂ TPD test. Notably, the Co(OH)₂-10%GR composite shows the most effective charge separation and transfer among these samples as reflected by EIS and PL spectra analysis (Supplementary Fig. 24c–e and Supplementary Table 5). However, because of the lowest CO₂ adsorption capacity of Co(OH)₂-10%GR composite (Supplementary Fig. 24a, b), its photocatalytic performance is inferior in diluted CO₂, which further confirms that CO₂ adsorption capacity is the crucial factor for affecting the photocatalytic performance of the catalysts.

The Mott-Schottky measurements in Supplementary Fig. 25a–c show that flat band potentials of Ni(OH)₂, GR, Ni(OH)₂-10%GR are ca. –0.7 V, –0.82 V and –0.76 V vs. normal hydrogen electrode (NHE), which are lower than that of E(Ru(bpy)₃)^{2+*/Ru(bpy)₃} = –1.09 V (vs. NHE) and higher than the redox potential of E(CO₂/CO) = –0.53 V (vs. NHE)^{54,55}. Hence, Ni(OH)₂, GR and Ni(OH)₂-10%GR all have suitable redox potential and can receive electrons from the reduced Ru complex to drive the photocatalytic CO₂-to-CO reduction reaction. In addition, the energy level diagram illustrated in Supplementary Fig. 25d indicates that the Fermi level (E_F) value of GR is lower than the lowest unoccupied molecular orbital (LUMO) value of [Ru(bpy)₃]Cl₂ and higher than the E_F value of Ni(OH)₂ (Supplementary Note 12). Therefore, the high carrier mobility and well-aligned energy levels of GR enable it to efficiently facilitate electron transfer from photosensitizers to Ni(OH)₂^{51,56}. On the basis of the above analysis, a possible reaction mechanism for the CO₂ photoreduction over Ni(OH)₂-10%GR composite has been proposed. As shown in Fig. 4f, under visible-light irradiation, the [Ru(bpy)₃]²⁺ photosensitizer is activated to the excited state [Ru(bpy)₃]^{2+*}, which is then reductively quenched by TEOA, forming the reduced photosensitizer [Ru(bpy)₃]⁺⁴⁴. Meanwhile, TEOA is oxidized to diethanolamine and glycolaldehyde^{57,58}. Subsequently, the reduced photosensitizer [Ru(bpy)₃]⁺ transfers electrons to GR, which further relays the electron to Ni(OH)₂. Finally, the adsorbed CO₂ on the Ni(OH)₂ surface are activated and reduced to CO. At the same time, parts of excited electrons are accepted by protons to produce H₂^{7,55}. The strong CO₂ affinity and weak H⁺ affinity of Ni sites endow Ni(OH)₂ with great potential for CO₂ uptake, thus promoting CO₂-to-CO conversion and inhibiting the generation of H₂ byproduct. In addition, compositing Ni(OH)₂ with GR to construct hierarchical nanosheet array structures can synergistically expose abundant active sites for photocatalytic CO₂ reduction, improve

CO₂ adsorption and promote separation and transfer of charge carriers. Therefore, Ni(OH)₂-10%GR composite displays the optimal photocatalytic CO₂ reduction performance as compared to that of other counterparts, including bare Ni(OH)₂, Ni(OH)₂ NPs-GR, Fe(OH)₃-GR, Cu(OH)₂-GR and Co(OH)₂-GR.

Discussion

In summary, we have rationally synthesized a series of transition metal hydroxides, including Ni(OH)₂, Fe(OH)₃, Cu(OH)₂, and Co(OH)₂, on the GR platform to act as cocatalysts for artificial photoreduction of CO₂. Specifically, hierarchical Ni(OH)₂ nanosheet arrays-graphene (Ni(OH)₂-GR) composites exhibit superior photocatalytic activity and selectivity. With the Ru-dye visible-light photosensitizer, the optimal Ni(OH)₂-10%GR composite exhibits a CO formation rate of 10725 μmol h^{–1} g^{–1} with selectivity of 96%. Even in the diluted CO₂, Ni(OH)₂-10%GR composite still exhibits excellent photoactivity with the CO generation rate of 7432 μmol h^{–1} g^{–1} and high selectivity of 92%, which is markedly higher than that of other counterparts. A series of complementary characterizations suggest that the synergy of enhanced CO₂ adsorption capacity, increased surface active sites, and improved charge separation/transfer of Ni(OH)₂-10%GR composite leads to its boosted optimal performance for photocatalytic CO₂ reduction as compared to that of other counterparts. It is expected that our current work could exploit new frontiers for the rational construction of earth-abundant transition metal hydroxides-based cocatalysts on graphene and other 2D material platforms for efficient and selective photoreduction of CO₂ to value-added chemical feedstocks.

Methods

Materials. Hydrochloric acid (HCl), nickel nitrate hexahydrate (Ni(NO₃)₂·6H₂O), triethanolamine (C₆H₁₅O₃N, TEOA), sulfuric acid (H₂SO₄), cobalt nitrate hexahydrate (Co(NO₃)₂·6H₂O), acetonitrile (CH₃CN, MeCN), deuterium oxide (D₂O), copper nitrate trihydrate (Cu(NO₃)₂·3H₂O), hexamethylenetetramine (C₆H₁₂N₄, HMTA), hydrogen peroxide (H₂O₂), iron nitrate nonahydrate (Fe(NO₃)₃·9H₂O), potassium permanganate (KMnO₄), trisodium citrate (C₆H₅O₇Na₃) and urea (CH₄N₂O) were supplied by Sinopharm Chemical Reagent Co., Ltd. (Shanghai, China). Cis-Dichlorobis(2,2-bipyridine)ruthenium (II) ([Ru(bpy)₂]Cl₂) were purchased from Sigma-Aldrich Co., Ltd (Shanghai, China). All chemicals were analytical grade and used as received. Deionized (DI) water was obtained from local sources.

Catalyst preparation. *Synthesis of graphene oxide:* GO was synthesized by a modified Hummers' method^{34,59–62}. In detail, 10 g graphite powder (supplied from Qingdao Zhongtian Company, China) was put into 230 mL concentrated H₂SO₄ under moderate stirring. Then, 30 g KMnO₄ was added gradually under stirring and the solution was cold below 5 °C in an ice bath. After that, the solution was heated to 35 °C in a water-bath and kept stirring for 2 h. Then, the mixture was diluted with 500 mL DI water in an ice bath to keep the temperature below 5 °C. Shortly after the further diluted with 1.5 L of DI water, 80 mL 30% H₂O₂ was then added into the mixture. The mixture was centrifuged and washed with 1:10 HCl aqueous solution to remove metal ions followed by DI water to remove the acid. After that, the mixture was dialyzed for one week and the final GO sample was obtained after full sonication.

Synthesis of nickel hydroxide nanosheet arrays-graphene (Ni(OH)₂-GR) composites: firstly, a certain amount of GO was dispersed into 50 mL DI water with ultrasonication for 1 h. Then, 2.5 mmol Ni(NO₃)₂·6H₂O was dissolved into the GO solution and stirred for 0.5 h. Afterward, a 50 mL solution containing 0.25 mmol of C₆H₅O₇Na₃ and 2.5 mmol of HMTA was incorporated to the above-mixed solution and stirred for 1 h. After that, the obtained solution was heated to 363 K and maintained for 10 h with vigorous agitation. Subsequently, when the solution temperature was cooled to 298 K, the sample was collected by centrifugation and washed thoroughly with DI water. After finally treated by freeze-drying, Ni(OH)₂-GR composites with different contents of GR (1, 5, 10, 30, and 50 wt%) were obtained. Other transition metal hydroxide-graphene composites (Co(OH)₂-GR, Fe(OH)₃-GR and Cu(OH)₂-GR) were prepared according to the same protocol as that for Ni(OH)₂-GR composite except for using the same amount of the corresponding transition metal nitrate instead. In comparison, blank Ni(OH)₂, Co(OH)₂, Fe(OH)₃, and Cu(OH)₂ were prepared using the identical process without GR platform. In addition, bare GR was prepared using the same method in the absence of transition metal nitrate.

Preparation of nickel hydroxide nanoparticles-graphene (Ni(OH)₂ NPs-GR) composite: Ni(OH)₂ NPs-10%GR composite was synthesized by a simple hydrothermal method^{18,63}. Typically, 2 mmol Ni(NO₃)₂·6H₂O, 6 mg GO and 250 mg of urea were dispersed into 30 mL DI water with ultrasonication for 1 h. After that, the mixed solution was added into a 50 mL Teflon-lined autoclave. The hydrothermal treatment was performed at 363 K for 10 h. When the temperature of solution was reduced to 298 K, the product was gathered by centrifugation, washed thoroughly with DI water, and treated by freeze-drying.

Characterization. The structures of the samples were determined by dual beam SEM (Helios G4 CX) and TEM (FEI Tecnai G2 F20). AFM measurements were performed in Agilent 5500 AFM (Agilent Technologies, USA). XRD patterns were collected on a Rigaku Miniflex diffractometer with Cu K α radiation. Thermogravimetric (TG) analysis was carried out on a PerkinElmer TGA7 analyzer under air atmosphere. BET surface areas and CO₂ adsorption capacity of the as-prepared samples were evaluated by Micromeritics TriStar II PLUS 3020 equipment at 77 and 298 K, respectively. CO₂ TPD measurements were performed on Micromeritics Auto Chem II 2920 instrument. XPS tests were executed on Thermo Scientific Escalab 250Xi spectrometer. Raman spectra were tested on a Renishaw inVia Raman System 1000 with a 532 nm Nd:YAG excitation source. Zeta-potentials (ζ) test was performed on Zetasizer 3000HSA. ¹H nuclear magnetic resonance (¹H NMR) measurement was conducted on Bruker DPX 400 spectrometer. Steady-state PL spectra and PL lifetime of these samples were tested on Edinburgh FLS-920 spectrofluorometer. The above PL measurements were performed in MeCN/H₂O/TEOA (3:2:1, 6 mL) mixed solution containing 7.5 mg Ru-dye and 1 mg as-prepared cocatalysts. The excitation wavelength was 405 nm when steady-state PL was measured. For the test of PL lifetime, the light source was 405 nm laser and the emission wavelength was 630 nm. EIS and Mott-Schottky measurements were implemented on electrochemical workstation (Autolab PGSTAT204).

Photocatalytic CO₂ reduction testing. MeCN/H₂O/TEOA (3:2:1, 6 mL) mixed solution containing 7.5 mg [Ru (bpy)₃]Cl₂·6H₂O photosensitizer and 1 mg as-prepared cocatalysts was added into a gas-closed quartz reactor. Then, the quartz reactor was purged with CO₂ (99.9999% or 10%) for 30 min. A 300 W Xe lamp (PLS-SXE300D, Perfectlight) with UV cutoff filter ($\lambda \geq 420$ nm) was applied to as the light source and the light intensity was measured to be 405 mW cm⁻². The reactor temperature was held at room temperature by an electronic fan. For each 2 h, the gaseous products were analysed by gas chromatography (GC 2014C, Shimadzu). H₂ was analyzed by a thermal conductivity detector (TCD). CO was converted to CH₄ using a methanation reactor and then detected by a flame ionization detector (FID). The liquid products were analysed using ¹H NMR. Isotope test was conducted by gas chromatography-mass spectrometry (GC-MS, 7890B and 5977 A, Agilent). The AQE was calculated according to the equation: AQE = [(2 × number of CO evolved molecules)/(number of incident photons)] × 100%. The turnover number (TON) for CO over Ru atoms was calculated using the following equation: TON = moles of CO evolved/moles of Ru atoms on photocatalyst. For recycling tests, the sample was collected and rinsed with DI water three times after 2 h of photocatalytic reaction. Then, the fresh reaction solution containing 7.5 mg Ru-dye was mixed with the used cocatalysts to conduct the second cycle experiment. By analogy, the subsequent four recycling tests were conducted.

Data availability

The data that support the findings of this study are available from the corresponding author on request. Source data are provided with this paper.

Received: 30 March 2020; Accepted: 11 September 2020;

Published online: 14 October 2020

References

- Zhang, N. et al. Waltzing with the versatile platform of graphene to synthesize composite photocatalysts. *Chem. Rev.* **115**, 10307–10377 (2015).
- Li, X. et al. Cocatalysts for selective photoreduction of CO₂ into solar fuels. *Chem. Rev.* **119**, 3962–4179 (2019).
- Collado, L. et al. Unravelling the effect of charge dynamics at the plasmonic metal/semiconductor interface for CO₂ photoreduction. *Nat. Commun.* **9**, 1–10 (2018).
- Wang, S. et al. Porous hypercrosslinked polymer-TiO₂-graphene composite photocatalysts for visible-light-driven CO₂ conversion. *Nat. Commun.* **10**, 676 (2019).
- Li, K., Peng, B. & Peng, T. Recent advances in heterogeneous photocatalytic CO₂ conversion to solar fuels. *ACS Catal.* **6**, 7485–7527 (2016).
- Dong, C. et al. Size-dependent activity and selectivity of carbon dioxide photocatalytic reduction over platinum nanoparticles. *Nat. Commun.* **9**, 1252 (2018).
- Han, B. et al. Nickel metal-organic framework monolayers for photoreduction of diluted CO₂: metal-node-dependent activity and selectivity. *Angew. Chem. Int. Ed.* **57**, 16811–16815 (2018).
- Zhong, W. et al. A covalent organic framework bearing single Ni sites as a synergistic photocatalyst for selective photoreduction of CO₂ to CO. *J. Am. Chem. Soc.* **141**, 7615–7621 (2019).
- Niu, K. et al. A spongy nickel-organic CO₂ reduction photocatalyst for nearly 100% selective CO production. *Sci. Adv.* **3**, e1700921 (2017).
- Chen, S. et al. Surface strategies for particulate photocatalysts toward artificial photosynthesis. *Joule* **2**, 2260–2288 (2018).
- Chang, X., Wang, T. & Gong, J. CO₂ photo-reduction: insights into CO₂ activation and reaction on surfaces of photocatalysts. *Energy Environ. Sci.* **9**, 2177–2196 (2016).
- Wang, S., Guan, B. Y. & Lou, X. W. Rationally designed hierarchical N-doped carbon@NiCo₂O₄ double-shelled nanoboxes for enhanced visible light CO₂ reduction. *Energy Environ. Sci.* **11**, 306–310 (2018).
- Lin, X. et al. Magnetic hollow spheres assembled from graphene-encapsulated nickel nanoparticles for efficient photocatalytic CO₂ reduction. *ACS Appl. Energy Mater.* **2**, 7670–7678 (2019).
- Ferrando, R., Jellinek, J. & Johnston, R. L. Nanoalloys: from theory to applications of alloy clusters and nanoparticles. *Chem. Rev.* **108**, 845–910 (2008).
- Vasileff, A. et al. Surface and interface engineering in copper-based bimetallic materials for selective CO₂ electroreduction. *Chem.* **4**, 1809–1831 (2018).
- Xiong, J. et al. Ultrathin structured photocatalysts: a versatile platform for CO₂ reduction. *Appl. Catal. B* **256**, 117788 (2019).
- Meng, A. et al. Hierarchical TiO₂/Ni(OH)₂ composite fibers with enhanced photocatalytic CO₂ reduction performance. *J. Mater. Chem. A* **6**, 4729–4736 (2018).
- Tang, T. et al. Kinetically controlled coprecipitation for general fast synthesis of sandwiched metal hydroxide nanosheets/graphene composites toward efficient water splitting. *Adv. Funct. Mater.* **28**, 1704594 (2018).
- Grote, F. et al. Self-stacked reduced graphene oxide nanosheets coated with cobalt-nickel hydroxide by one-step electrochemical deposition toward flexible electrochromic supercapacitors. *Small* **11**, 4666–4672 (2015).
- Yang, M.-Q. et al. Artificial photosynthesis over graphene-semiconductor composites. Are we getting better? *Chem. Soc. Rev.* **43**, 8240–8254 (2014).
- Yang, M.-Q. & Xu, Y.-J. Photocatalytic conversion of CO₂ over graphene-based composites: current status and future perspective. *Nanoscale Horiz.* **1**, 185–200 (2016).
- Ong, W.-J. et al. Graphene oxide as a structure-directing agent for the two-dimensional interface engineering of sandwich-like graphene-g-C₃N₄ hybrid nanostructures with enhanced visible-light photoreduction of CO₂ to methane. *Chem. Commun.* **51**, 858–861 (2015).
- Yang, M.-Q. et al. Ultrathin nickel boron oxide nanosheets assembled vertically on graphene: a new hybrid 2D material for enhanced photo/electrocatalysis. *Mater. Horiz.* **4**, 885–894 (2017).
- Ma, Y. et al. Homogeneous metal nitrate hydroxide nanoarrays grown on nickel foam for efficient electrocatalytic oxygen evolution. *Small* **14**, 1803783 (2018).
- Sun, Z. et al. Catalysis of carbon dioxide photoreduction on nanosheets: fundamentals and challenges. *Angew. Chem. Int. Ed.* **57**, 7610–7627 (2018).
- Hou, W., Xiao, Y. & Han, G. An interconnected ternary Mn₂S₄ (M = Fe, Co, Ni) thiospinel nanosheet array: a type of efficient platinum-free counter electrode for dye-sensitized solar cells. *Angew. Chem. Int. Ed.* **56**, 9146–9150 (2017).
- Kim, D. et al. Synergistic geometric and electronic effects for electrochemical reduction of carbon dioxide using gold-copper bimetallic nanoparticles. *Nat. Commun.* **5**, 4948 (2014).
- Nagaraju, G., Cha, S. M. & Yu, J. S. Ultrathin nickel hydroxide nanosheet arrays grafted biomass-derived honeycomb-like porous carbon with improved electrochemical performance as a supercapacitive material. *Sci. Rep.* **7**, 45201 (2017).
- Lin, H. & Wang, X. Epitaxy of radial high-energy-faceted ultrathin TiO₂ nanosheets onto nanowires for enhanced photoreactivities. *Adv. Funct. Mater.* **26**, 1580–1589 (2016).
- Wei, G. et al. Carbon quantum dot-induced self-assembly of ultrathin Ni(OH)₂ nanosheets: a facile method for fabricating three-dimensional porous hierarchical composite micro-nanostructures with excellent supercapacitor performance. *Nano Res.* **10**, 3005–3017 (2017).
- Fan, H. et al. Controllable synthesis of ultrathin transition-metal hydroxide nanosheets and their extended composite nanostructures for enhanced catalytic activity in the heck reaction. *Angew. Chem. Int. Ed.* **55**, 2167–2170 (2016).
- Hussain, N. et al. Ultrathin mesoporous F-doped α -Ni(OH)₂ nanosheets as an efficient electrode material for water splitting and supercapacitors. *J. Mater. Chem. A* **7**, 9656–9664 (2019).
- Lee, J. W., Ko, J. M. & Kim, J.-D. Hierarchical microspheres based on α -Ni(OH)₂ nanosheets intercalated with different anions: synthesis, anion

- exchange, and effect of intercalated anions on electrochemical capacitance. *J. Phys. Chem. C* **115**, 19445–19454 (2011).
34. Lu, K.-Q. et al. Rational utilization of highly conductive, commercial elicarb graphene to advance the graphene-semiconductor composite photocatalysis. *Appl. Catal. B* **224**, 424–432 (2018).
35. Jia, D. et al. Hierarchical α -Ni(OH)₂ composed of ultrathin nanosheets with controlled interlayer distances and their enhanced catalytic performance. *ACS Appl. Mater. Interfaces* **9**, 20476–20483 (2017).
36. Li, Y. et al. Effective catalytic reduction of 4-nitrophenol to 4-aminophenol over etched halloysite nanotubes@ α -Ni(OH)₂. *ACS Appl. Energy Mater.* **3**, 4756–4766 (2020).
37. Xie, J. et al. Copper-incorporated hierarchical wire-on-sheet α -Ni(OH)₂ nanoarrays as robust trifunctional catalysts for synergistic hydrogen generation and urea oxidation. *J. Mater. Chem. A* **7**, 13577–13584 (2019).
38. Bag, S. & Raj, C. R. Layered inorganic-organic hybrid material based on reduced graphene oxide and α -Ni(OH)₂ for high performance supercapacitor electrodes. *J. Mater. Chem. A* **2**, 17848–17856 (2014).
39. Weng, B. et al. Toward the enhanced photoactivity and photostability of ZnO nanospheres via intimate surface coating with reduced graphene oxide. *J. Mater. Chem. A* **2**, 9380–9389 (2014).
40. Lu, K.-Q. et al. Insight into the origin of boosted photosensitive efficiency of graphene from the cooperative experiment and theory study. *J. Phys. Chem. C* **120**, 27091–27103 (2016).
41. Ke, Q. et al. 3D TiO₂@Ni(OH)₂ core-shell arrays with tunable nanostructure for hybrid supercapacitor application. *Sci. Rep.* **5**, 13940 (2015).
42. Wang, H. et al. Ni(OH)₂ nanoplates grown on graphene as advanced electrochemical pseudocapacitor materials. *J. Am. Chem. Soc.* **132**, 7472–7477 (2010).
43. Ouyang, T. et al. A dinuclear cobalt cryptate as a homogeneous photocatalyst for highly selective and efficient visible-light driven CO₂ reduction to CO in CN₃CN/H₂O solution. *Angew. Chem. Int. Ed.* **56**, 738–743 (2017).
44. Wang, Y., Wang, S. & Lou, X. W. Dispersed nickel cobalt oxyphosphide nanoparticles confined in multichannel hollow carbon fibers for photocatalytic CO₂ reduction. *Angew. Chem. Int. Ed.* **58**, 17236–17240 (2019).
45. Liu, W. et al. A scalable general synthetic approach toward ultrathin imine-linked two-dimensional covalent organic framework nanosheets for photocatalytic CO₂ reduction. *J. Am. Chem. Soc.* **141**, 17431–17440 (2019).
46. Wu, L. Y. et al. Encapsulating perovskite quantum dots in iron-based metal-organic frameworks (MOFs) for efficient photocatalytic CO₂ reduction. *Angew. Chem. Int. Ed.* **58**, 9491–9495 (2019).
47. Li, A. et al. Three-phase photocatalysis for the enhanced selectivity and activity of CO₂ reduction on a hydrophobic surface. *Angew. Chem. Int. Ed.* **58**, 14549–14555 (2019).
48. Tamaki, Y. & Ishitani, O. Supramolecular photocatalysts for the reduction of CO₂. *ACS Catal.* **7**, 3394–3409 (2017).
49. Kimura, E. et al. New series of multifunctionalized nickel (II)-cyclam (cyclam = 1,4,8,11-tetraazacyclotetradecane) complexes. Application to the photoreduction of carbon dioxide. *Inorg. Chem.* **33**, 770–778 (1994).
50. Zhu, W. et al. Selective reduction of CO₂ by conductive MOF nanosheets as an efficient co-catalyst under visible light illumination. *Appl. Catal. B* **238**, 339–345 (2018).
51. Gao, C. et al. Heterogeneous single-atom catalyst for visible-light-driven high-turnover CO₂ reduction: the role of electron transfer. *Adv. Mater.* **30**, 1704624 (2018).
52. Wang, X.-K. et al. Monometallic catalytic models hosted in stable metal-organic frameworks for tunable CO₂ photoreduction. *ACS Catal.* **9**, 1726–1732 (2019).
53. Weng, B. et al. Stabilizing ultrasmall Au clusters for enhanced photoredox catalysis. *Nat. Commun.* **9**, 1–11 (2018).
54. Schneider, J. et al. Thermodynamics and kinetics of CO₂, CO, and H⁺ binding to the metal centre of CO₂ reduction catalysts. *Chem. Soc. Rev.* **41**, 2036–2051 (2012).
55. Han, B. et al. Hierarchical NiCo₂O₄ hollow nanocages for photoreduction of diluted CO₂: Adsorption and active sites engineering. *Appl. Catal. B* **260**, 118208 (2020).
56. Mu, Q. et al. Electrostatic charge transfer for boosting the photocatalytic CO₂ reduction on metal centers of 2D MOF/rGO heterostructure. *Appl. Catal. B* **262**, 118144 (2020).
57. Zhu, Y. et al. Bimetallic Ag-Cu supported on graphitic carbon nitride nanotubes for improved visible-light photocatalytic hydrogen production. *ACS Appl. Mater. Interfaces* **10**, 9468–9477 (2018).
58. Du, P. et al. Photocatalytic generation of hydrogen from water using a platinum (II) terpyridyl acetylide chromophore. *J. Am. Chem. Soc.* **128**, 7726–7727 (2006).
59. Zhang, Y. et al. Engineering the unique 2D mat of graphene to achieve graphene-TiO₂ nanocomposite for photocatalytic selective transformation: what advantage does graphene have over its forebear carbon nanotube? *ACS Nano* **5**, 7426–7435 (2011).
60. Zhang, Y. et al. Graphene transforms wide band gap ZnS to a visible light photocatalyst. The new role of graphene as a macromolecular photosensitizer. *ACS Nano* **6**, 9777–9789 (2012).
61. Zhang, N. et al. Toward improving the graphene-semiconductor composite photoactivity via the addition of metal ions as generic interfacial mediator. *ACS Nano* **8**, 623–633 (2013).
62. Hummers, W. S. Jr. & Offeman, R. E. Preparation of graphitic oxide. *J. Am. Chem. Soc.* **80**, 1339–1339 (1958).
63. Chen, X et al. One-pot hydrothermal synthesis of reduced graphene oxide/carbon nanotube/ α -Ni(OH)₂ composites for high performance electrochemical supercapacitor. *J. Power Sour.* **243**, 555–561 (2013).

Acknowledgements

Y.-J.X. acknowledges the support from the NSFC (21872029, U1463204, 20903023, 21173045 and 22072023), the Award Program for Minjiang Scholar Professorship, the Independent Research Project of State Key Laboratory of Photocatalysis on Energy and Environment (NO. 2014A05), the Program for Leading Talents of Fujian Universities, the 1st Program of Fujian Province for Top Creative Young Talents, and the NSF of Fujian Province (2017J07002, 2019J0106).

Author contributions

Y.-J.X. proposed the research direction and supervised the project. K.Q.L. designed and performed the experiments. Y.H.L. and F.Z. performed XRD measurement and analysis. M.Y.Q. and X.C. carried out SEM characterization and analysis. Y.-J.X. and K.Q.L. wrote and revised the manuscript. Z.-R.T., Y.M.A.Y., M.A., and M.C. provided helpful suggestions. All authors participated in discussion and reviewed the paper before submission.

Competing interests

The authors declare no competing interests.

Additional information

Supplementary information is available for this paper at <https://doi.org/10.1038/s41467-020-18944-1>.

Correspondence and requests for materials should be addressed to Y.-J.X.

Peer review information *Nature Communications* thanks Hermenegildo Garcia and other, anonymous, reviewers for their contributions to the peer review of this work.

Reprints and permission information is available at <http://www.nature.com/reprints>

Publisher's note Springer Nature remains neutral with regard to jurisdictional claims in published maps and institutional affiliations.



Open Access This article is licensed under a Creative Commons Attribution 4.0 International License, which permits use, sharing, adaptation, distribution and reproduction in any medium or format, as long as you give appropriate credit to the original author(s) and the source, provide a link to the Creative Commons license, and indicate if changes were made. The images or other third party material in this article are included in the article's Creative Commons license, unless indicated otherwise in a credit line to the material. If material is not included in the article's Creative Commons license and your intended use is not permitted by statutory regulation or exceeds the permitted use, you will need to obtain permission directly from the copyright holder. To view a copy of this license, visit <http://creativecommons.org/licenses/by/4.0/>.

© The Author(s) 2020